RESEARCH

Biomass smoke inhalation promotes neuroinflammatory and metabolomic temporal changes in the hippocampus of female mice

David Scieszka[1], Yan Jin[2], Shahani Noor[3], Ed Barr[1], Marcus Garcia[1], Jessica Begay[1], Guy Herbert[1], Russell P. Hunter[1], Kiran Bhaskar[3], Rahul Kumar[4], Rama Gullapalli[4], Alicia Bolt[1], Mark A. McCormick[5], Barry Bleske[6], Haiwei Gu[2] and Matthew J. Campen[1*]

Abstract

Smoke from wildland fires has been shown to produce neuroinflammation in preclinical models, characterized by neural infiltrations of neutrophils and monocytes, as well as altered neurovascular endothelial phenotypes. To address the longevity of such outcomes, the present study examined the temporal dynamics of neuroinflammation and metabolomics after inhalation exposures from biomass-derived smoke. 2-month-old female C57BL/6 J mice were exposed to wood smoke every other day for 2 weeks at an average exposure concentration of 0.5 mg/m^3. Subsequent serial euthanasia occurred at 1-, 3-, 7-, 14-, and 28-day post-exposure. Flow cytometry of right hemispheres revealed two endothelial populations of CD31^{Hi} and CD31^{Med} expressors, with wood smoke inhalation causing an increased proportion of CD31^{Hi}. These populations of CD31^{Hi} and CD31^{Med} were associated with an anti-inflammatory and pro-inflammatory response, respectively, and their inflammatory profiles were largely resolved by the 28-day mark. However, activated microglial populations (CD11b$^+$/CD45^{low}) remained higher in wood smoke-exposed mice than controls at day 28. Infiltrating neutrophil populations decreased to levels below controls by day 28. However, the MHC-II expression of the peripheral immune infiltrate remained high, and the population of neutrophils retained an increased expression of CD45, Ly6C, and MHC-II. Utilizing an unbiased approach examining the metabolomic alterations, we observed notable hippocampal perturbations in neurotransmitter and signaling molecules, such as glutamate, quinolinic acid, and 5-α-dihydroprogesterone. Utilizing a targeted panel designed to explore the aging-associated NAD$^+$ metabolic pathway, wood smoke exposure drove fluctuations and compensations across the 28-day time course, ending with decreased hippocampal NAD$^+$ abundance on day 28. Summarily, these results indicate a highly dynamic neuroinflammatory environment, with potential resolution extending past 28 days, the implications of which may include long-term behavioral changes, systemic and neurological sequalae directly associated with wildfire smoke exposure.

Keywords Particulate matter, Wildfire smoke, Blood brain barrier, Neuroinflammation, Inhalation

*Correspondence:
Matthew J. Campen
mcampen@salud.unm.edu
Full list of author information is available at the end of the article

Scieszka *et al. Journal of Neuroinflammation*   (2023) 20:192

Page 2 of 15

Introduction

Wildland fire acres burned per year have roughly doubled since 1985 [1]. These fires now routinely generate smoke that deteriorates air quality for most of the country. This smoke contains a multifarious mixture of toxic components due to myriad combustion fuel sources (*e.g.*, biomass, homes, cars etc.). These wildfire exposures have been linked to cardiovascular [2], pulmonary [2, 3], ocular [4, 5], nasal [5], and recently neurological outcomes [6, 7].

Neuroinflammation following acute and subchronic exposures to wildfire smoke, along with other pollutants such as ozone and diesel emissions have been reported [8–11]. The neurological outcomes are postulated to arise from responses to pollutants in the lungs, with previous work positing that inhaled particulate matter (PM) induces pulmonary proteolysis, which in turn generates fragmented peptides that enter the circulation and impair the blood–brain barrier (BBB) integrity through endothelial receptor antagonism [6, 12–15]. Phenotypically, the BBB includes two separate populations of endothelial cells expressing differential levels of CD31 (aka platelet endothelial cell adhesion molecule-1, PECAM-1), with a proinflammatory phenotype coinciding with reduced relative CD31 [16, 17]. The BBB is a tightly connected system of endothelial cells and pericytes wrapped by astrocytic end-feet, ensuring a regulated separation between peripheral circulation and the central nervous system (CNS). When the lung-derived fragmented peptides arising from pollutant inhalation interact with neurovascular endothelial cells and cause these junctions to fail, current understanding dictates an upregulation of intercellular adhesion molecule-1 (ICAM-1) and chemokine C–C motif ligand 2 (CCL2), with additional downstream activation of resident astrocytes and microglia [12–15]. Previously, a 20-day exposure to naturally occurring wildfire smoke particles altered the distribution of the neurovascular endothelial cell phenotypes, with an increased proportion of CD31^{Hi} (anti-inflammatory) cells exhibiting a reduced level of CCL2, inducible nitric oxide synthase, and tumor necrosis factor-α (TNFα) following particle inhalation [6]. CD31^{Med} expressing endothelial cells, however, exhibited higher expression of those same inflammatory proteins, implying that the inflammatory response was mixed and exhibiting a switchover from induction to resolution.

Peripheral immune cells can express leukocyte function-associated antigen-1 (LFA-1) and interact with CCL2, which both act as transmigration signals for peripheral invasion into the neurological milieu. However, myeloid cells can also express CCL2 in response to stimuli [18]. In addition to CCL2, the vascular cell adhesion molecule-1 (VCAM-1) is recognized by peripheral immune cells for a trans-BBB migration effect, and further mediates peripheral immune invasion [19]. In addition, neutrophils can express lymphocyte antigen 6 complex (Ly6C), while activated microglia and microglial precursors can express the marker as well [20].

Previous studies have shown that wildfire smoke particulate matter exposure caused only modest pulmonary inflammation yet initiated numerous neuroinflammatory sequelae, including microglial activation, peripheral immune infiltration, and decreased neuroprotective metabolites [6, 7]. To better explore the timing of resolution of this neuroinflammation, we sought to replicate biomass smoke inhalation exposure in a lab setting. Using a serial euthanasia study design, we investigated the onset of inflammatory endothelial response and resolution of inflammation through flow cytometry and metabolomics approaches.

Materials and methods

Animals and exposures

Female C57BL/6 mice (Jackson Labs) at 8 weeks of age were housed in AAALAC-approved facilities, on a 12 h light:dark cycle and provided a standard chow diet and water ad libitum, in quarantine for 1 week of acclimation prior to exposure. The exclusive use of female C57BL/6J mice in our study was strategically chosen due to evidence of sex-based differences in inflammatory and metabolic responses, particularly relevant to neuroinflammation [21, 22]. This selection allows us to isolate sex-specific factors influenced by unique hormonal and genetic backgrounds, thereby providing a more refined exploration of the female response. In addition, our choice helps address a historical bias in research favoring male subjects, and thus fills a significant knowledge gap in female biological processes [23, 24]. Consequently, our decision aligns with both the specific scientific inquiry and broader principles of achieving comprehensive biological understanding. A total of 60 mice were used, randomly and evenly divided into filtered air (FA) control and woodsmoke (WS) exposed groups, with an $n=6$ per exposure per timepoint (Fig. 1). All procedures were conducted with approval by the University of New Mexico Institutional Animal Care and Use Committee. Exposures were conducted in BioSpherix Medium A-Chamber, with mice in reusable shoebox plastic animal case systems with standard wire tops; water was available to mice throughout the exposures, but food was withheld to avoid contamination of the food with biomass soot (4 h/d). Biomass smoke production was facilitated by a ceramic furnace surrounding a quartz tube connected to a dilution chamber, with subsequent plumbing into the exposure chamber [25]. Approximately 100 mg of
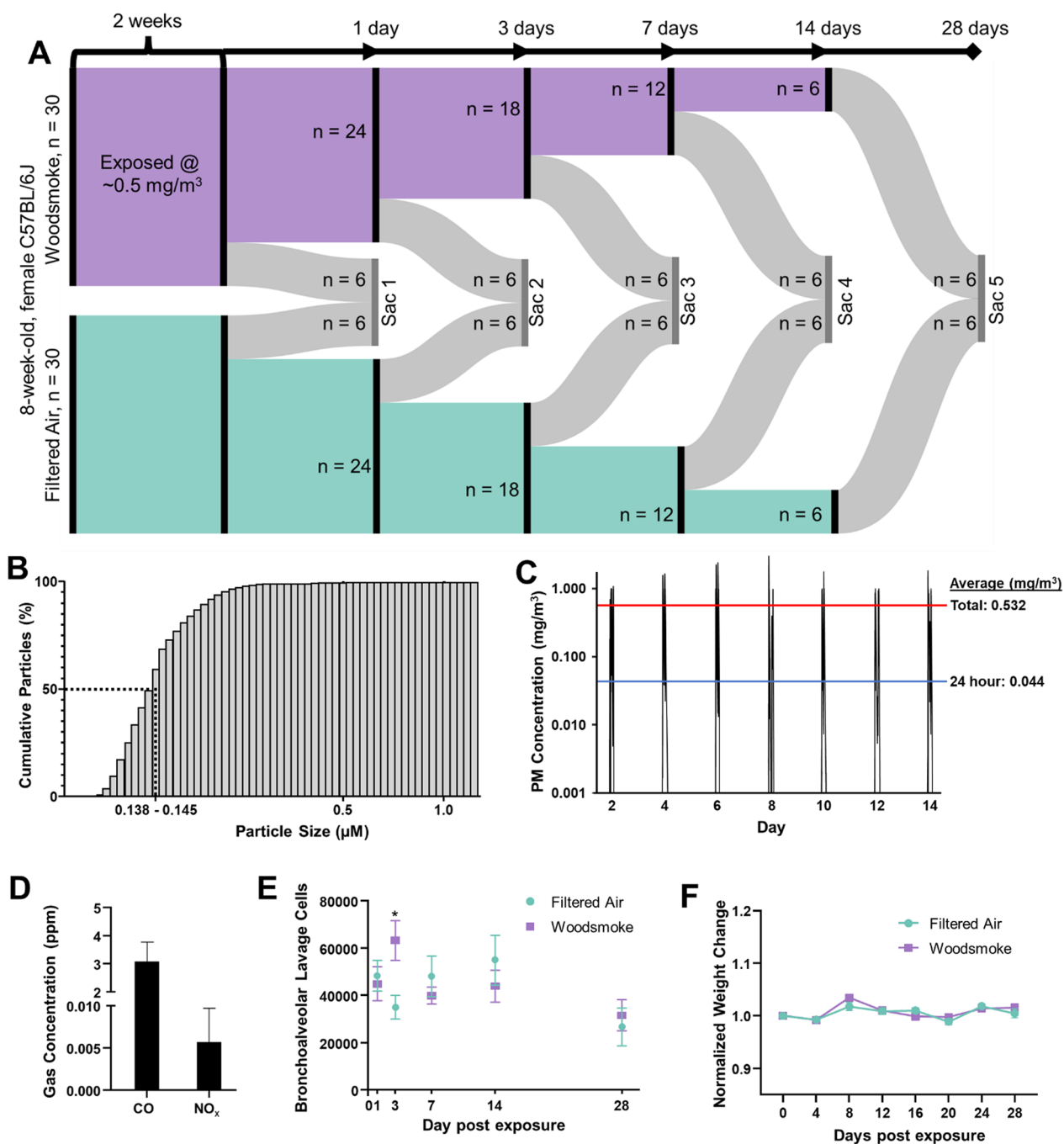
Scieszka *et al. Journal of Neuroinflammation*   (2023) 20:192

Page 3 of 15

Fig. 1 Study design and exposure characterization. **A** 8-week-old female C57BL/6J mice were exposed to woodsmoke derived from woodchip biomass every other day for 2 weeks at an exposure concentration average ~ 500 μg/m³ per exposure. After exposure, mice were euthanized at serial timepoints of 1-, 3-, 7-, 14-, and 28-day post-exposure. **B** Particle size distribution percentile curve. Median particle size measured between 0.138 μm and 0.145 μm. **C** Exposure averaged 532 μg/m³ for total exposure duration and 0.044 mg/m³ for 24-h average. Red line: exposure average per 4 h exposure. Blue line: exposure average considering 24 h per day. **D** Biomass-derived carbon monoxide (CO) and oxides of nitrogen species (NO_x) concentrations (both below USEPA standards). **E** Bronchoalveolar lavage fluid was extracted for cell staining and differential analyses. Total cells were statistically increased in the lung on day 3, but no other differences were seen for other cells or on other days. **F** No significant weight differences were seen between groups for the duration of experimentation

Scieszka *et al. Journal of Neuroinflammation*   (2023) 20:192

Page 4 of 15

piñon wood chips were used per 4 h exposure. Smoke exposure was facilitated by vacuum and/or pressurization, with total pressure monitoring to ensure min/max pressure never exceeded $-/+25$ mm Hg within the exposure chamber. Concentrations were adjusted manually to ensure a consistent range of WS, using a dump vacuum/pressurizing pump to remove smoke from the exposure chamber or vacuum/pressurizing pumps to channel more smoke from the biomass burning tube into the dilution chamber or reduce flow from the dilution chamber. Mice were exposed whole-body for 4 h every other day for 14 days. We elected this exposure paradigm to mimic intermittent exposure to wood smoke, which aligns more closely with real-world exposure scenarios while mitigating the potential stress of daily exposure. This duration and frequency were also chosen based on previous research demonstrating significant yet non-lethal physiological alterations within similar timelines, allowing us to study the temporal dynamics and resolution of the resultant neuroinflammation and metabolic disturbances [6]. After the last round of exposures, groups of mice were euthanized intermittently over a 28-day period with 6 FA and 6 exposed mice euthanized 1-, 3-, 7-, 14-, and 28-day post-exposure (Fig. 1A–C).

Bronchoalveolar lavage collection

To obtain bronchoalveolar lavage fluid, the whole lung was flushed with 800 µl of Dulbecco's phosphate buffered saline (PBS). Post-lavage, the sample was centrifuged to separate cells and liquid supernatant. The supernatant was immediately frozen in liquid nitrogen at -80 °C for later analysis. The cell pellet was resuspended and used to prepare cytospin slides. These slides were fixed and stained using a modified Wright–Giemsa protocol. Stained slides were then examined by hemocytometer for quantitative differential counting of cell populations.

Particulate matter characterization

Exposure concentrations were measured in real time from a sampling tube positioned centrally in the exposure chamber with a DustTrak II (TSI, Inc; Shoreview, Minnesota) and gravimetrically using 47 mm quartz filter collected for the duration of each daily exposure and weighed on a microbalance (XPR6UD5, Mettler Toledo) in a temperature-controlled laboratory. Particle size distribution was quantified for the overall system prior to mouse exposures (Laser Aerosol Spectrometer 3340A, TSI), again sampling directly from the center of

the exposure chamber. Size distribution was measured over a single 2-h run (0.138–0.145 µg; Fig. 1B).

Brain tissue digestion for flow cytometry

Under isoflurane anesthesia, all 12 mice per timepoint underwent transcardial ice-cold 0.1 M PBS (pH=7.4) perfusion. Hippocampus samples were dissected from the left hemisphere for metabolomics analysis (below), and all portions of the left hemisphere were flash-frozen in liquid N_2. Right hemispheres from all mice were used for flow cytometry. For flow cytometry, tissues were harvested in ice-cold HBSS buffer and processed immediately according to Miltenyi gentleMACS™ adult neural tissue digestion protocol, as described [6, 26]. Briefly, brain tissues were minced with fine-tip scissors and processed with enzymatic and mechanical digestion steps with gentleMACS™ Octo dissociator with heaters (Miltenyi Biotec, CA, USA). Following digestion steps, cell suspensions were passed through 70 µm cell strainers. Myelin debris was removed with Debris Removal Solution (Miltenyi Biotec, CA, USA, 130-109-398), according to the manufacturer's protocol. Cells were resuspended in PBS (without calcium and magnesium, Sigma-Aldrich, St. Louis, MO) and kept on ice until proceeding to viability dye staining.

Cell staining for surface and intracellular antigens for flow cytometry

For flow cytometry analysis, live cells were counted on a hemocytometer using trypan blue staining exclusion criteria. Between 0.2 and 1.0×10^6 cells were transferred in fluorescence activated cell sorting (FACs) tubes, stained with viability dye eFlour 450 (eBioscience, San Diego, CA) for 30 min. After a wash with FACs buffer ($1 \times PBS$ containing 0.5% bovine serum albumin and 1 mM EDTA) and incubation with a saturating solution of Fc block (BD Biosciences, San Jose, CA, USA), cells were stained for surface antigens for 25 min in the dark on ice. Antibodies against mouse CD11b, CD45, MHC-II, and CD31 were all purchased from Thermo Fisher Scientific, MA, USA and used as 0.125–0.5 µg/10^6 cells, as recommended by the manufacturer. Cells were examined for intracellular levels of various proinflammatory factors: TNFα, CCL2 and inducible nitric oxide synthase (iNOS). For intracellular staining, cells were fixed with fixation buffer and then permeabilized using intracellular fixation and permeabilization buffer (eBioscience, USA). Cells were then stained with fluorochrome conjugated-antibodies for the intracellular immune factors for another 1 h at room temperature in the dark. After another wash with $1 \times$ permeabilization buffer, cells were resuspended in 250–300 µl FACs buffer and immediately quantified in the flow cytometer. At least 50,000 live cell events were

collected for each sample. Single-stained controls and isotype controls were used for laser compensation and data analysis. Data were acquired using the BD LSR Fortessa cell analyzer (BD Biosciences, San Jose, CA) and analyzed using Flow Jo software v10.7.1.

Flow cytometry gating strategy

The gating strategy for determining different cell subsets in the brain tissues is similar to that described in our prior reports [6, 26]. Briefly, doublets (cell clumps) were excluded, and the live cells were identified based on their size, granularity (FSC v SSC) and negative viability dye staining. Cerebrovascular endothelial cells were identified based on negative expression of the common leukocyte marker, CD45 and positive staining for CD31(Platelet endothelial cell adhesion molecule-1, PECAM-1). All CD45 + cells were first gated for peripheral mononuclear neutrophil (PMN) or neutrophil marker, Ly6G (1A8) staining, which were also verified by their positive CD11b staining. The population of CD45 + 1A8–(leukocytes that are not neutrophils) was further analyzed to identify microglia with low or medium expression of CD45 (CD45 low/med, CD11b +) as distinguished from infiltrating macrophages/monocytes with CD45^{Hi} expression (CD45^{Hi} CD11b +). Activated microglia were distinguished from non-activated microglia based on combined expression levels of CD45 and CD11b [27]. In addition, infiltrating monocytes/macrophages were further analyzed for Ly6C expression to identify inflammatory monocytes (1A8–CD11b + CD45^{Hi} Ly6C +). Median or geometric mean fluorescent intensities were plotted for activation markers or cytokine expression on these different immune and endothelial cell subsets.

Metabolomics tissue preparation and analysis

Briefly, each hippocampus sample (~ 20 mg, n = 6) was homogenized in 200 µL MeOH:PBS (4:1, v:v, containing 1,810.5 µM $^{13}C_3$-lactate and 142 µM $^{13}C_5$-glutamic acid) in an Eppendorf tube using a Bullet Blender homogenizer (Next Advance, Averill Park, NY). Then, 800 µL MeOH:PBS (4:1, v:v, containing 1810.5 µM $^{13}C_3$-lactate and 142 µM $^{13}C_5$-glutamic Acid) was added and, after vortexing for 10 s, the samples were stored at − 20 °C for 30 min. The samples were then sonicated in an ice bath for 30 min. The samples were centrifuged at 14,000 RPM for 10 min (4 °C), and 800 µL of supernatant was transferred to a new Eppendorf tube. The samples were then dried under vacuum using a CentriVap Concentrator (Labconco, Fort Scott, KS). Prior to mass spectrometry analysis, the obtained residue was reconstituted in 150 µL 40% PBS/60% acetonitrile. A quality control sample was pooled from all the study samples.

Targeted liquid chromatography–tandem mass spectrometry (LC–MS/MS) technique was used to measure NAD$^+$ metabolites, and it is similar to several recent reports (Carroll et al. 2015; Eghlimi et al. 2020; Gu et al. 2016; Gu et al. 2015; Jasbi et al. 2019; Shi et al. 2019). Briefly, LC–MS/MS experiments were performed on an Agilent 1290 UPLC-6490 QQQ–MS (Santa Clara, CA) system. Each hippocampus sample was injected twice: first a 10 µL volume for analysis using negative ionization mode and second a 4 µL volume for analysis using positive ionization mode. Both chromatographic separations were performed in hydrophilic interaction chromatography mode on a Waters XBridge BEH Amide column (150 × 2.1 mm, 2.5 µm particle size, Waters Corporation, Milford, MA). The flow rate was 0.3 mL/min, auto-sampler temperature was kept at 4ºC, and the column compartment was set at 40 °C. The mobile phase was composed of Solvents A (10 mM ammonium acetate, 10 mM ammonium hydroxide in 95% H_2O/5% acetonitrile) and B (10 mM ammonium acetate, 10 mM ammonium hydroxide in 95% acetonitrile/5% H_2O). After the initial 1 min isocratic elution of 90% B, the percentage of Solvent B decreased to 40% at t = 11 min. The composition of Solvent B maintained at 40% for 4 min (t = 15 min), and then the percentage of B gradually went back to 90%, to prepare for the next injection. The mass spectrometer is equipped with an electrospray ionization source. Targeted data acquisition was performed in multiple-reaction-monitoring mode. The whole LC–MS system was controlled by Agilent Masshunter Workstation software (Santa Clara, CA). The extracted MRM peaks were integrated using Agilent MassHunter Quantitative Data Analysis (Santa Clara, CA). Resultant data were normalized by tissue weight before subsequent normalization steps.

The untargeted LC–MS metabolomics method used here was modeled after that developed and used in a growing number of studies [28–31]. Briefly, all LC–MS experiments were performed on a Thermo Vanquish UPLC-Exploris 240 Orbitrap MS instrument (Waltham, MA). The LC conditions were the same as those in targeted metabolomics. Using mass spectrometer equipped with an electrospray ionization (ESI) source, we will collect untargeted data from 70 to 1050 m/z. To identify peaks from the MS spectra, we made extensive use of the in-house chemical standards (~ 600 aqueous metabolites), and in addition, we searched the resulting MS spectra against the HMDB library, Lipidmap database, METLIN database, as well as commercial databases including mzCloud, Metabolika, and ChemSpider. The absolute intensity threshold for the MS data extraction was 1,000, and the mass accuracy limit was set to 5 ppm. Identifications and annotations used available data for

Scieszka *et al. Journal of Neuroinflammation*　　(2023) 20:192

Page 6 of 15

retention time (RT), exact mass (MS), MS/MS fragmentation pattern, and isotopic pattern. We used the Thermo Compound Discoverer 3.3 software for aqueous metabolomics data processing. The untargeted data were processed by the software for peak picking, alignment, and normalization. To improve rigor, only the signals/peaks with CV < 20% across quality control (QC) pools, and the signals showing up in > 80% of all the samples were included for further analysis.

Data analysis and statistics

Quality control samples were inserted at 10-sample intervals during mass spectrometry measurement and were utilized as a pooled sample group to compensate for temporal variability on the machine. Data were analyzed using the R package MetaboAnalyst 5.0 [32, 33]. Normality was determined via Shapiro–Wilk testing. In the event of normally distributed data, Student's *t* tests were used. For non-normally distributed data, *t* tests were employed on $\log_2()$ transformed data based on right-tailed distribution. Tests were either conducted in GraphPad Prism v9.1.1, Excel (Version 2211 Build 16.0.15831.20098) or RStudio v1.4.1564, R v4.3.4. Venn diagram was generated using an online multiple list comparison tool [34], with Jaccard ratios calculated via the same software. Student's *t* tests were performed on the data sets and uncorrected as these data were not individually examined, but qualitatively explored as overlapping matrices. These values were input into Excel, RStudio, or downloaded directly for figure generation. Volcano plots were generated using a raw $p < 0.05$ (NAD$^+$ panel; < 20 total metabolites) or FDR corrected $p < 0.1$ (untargeted panel), both with fold-change > 1.5. Heatmapping was performed using limma-based linear regression[35] (untargeted) or interquartile variance (NAD$^+$) with metabolite number explicitly stated in the figure legends.

Results

Exposure characterization

8-week-old female C57BL/6 J mice were exposed to wood smoke every other day at an average exposure concentration of 0.5 mg/m^3 for 2 weeks (24 h: 0.44 mg/m^3, Fig. 1 A–D). Subsequent serial euthanasia occurred at 1-, 3-, 7-, 14-, and 28-day post-exposure (Fig. 1A). Exposure-measured carbon monoxide (CO) and oxides of nitrogen species (NO$_X$) were below the USEPA standards (Fig. 1D). Bronchoalveolar lavage samples were taken at each euthanasia timepoint (Fig. 1E) with total cells significantly higher on day 3 post-exposure, but no other differences were seen for other cells (neutrophils, lymphocytes, eosinophils) or on different days. Weight was monitored throughout the study, with no significant separations or deviations observed (Fig. 1F).

Cerebrovascular endothelial cell neuroinflammatory activation and resolution in response to woodsmoke

A list of *p* values can be found in Table 1. After gating, we observed two distinct populations of endothelial cells expressing a range of PECAM (Fig. 2), consistent with our previous study of real-world wildfire smoke [6]. The population of CD31^{Hi} was significantly increased from day 1 (D1) post-exposure until day 14 (D14; Fig. 2A). The percentage of cells on each day relative to total cells is as follows (D[x^{marker}]: FA%/WS%). D1^{CD31Hi}: 1.64/3.05, D1^{CD31Med}: 17.73/8.30, D3^{CD31Hi}: 2.28/3.99, D3^{CD31Med}: 3.09/1.58, D7^{CD31Hi}: 0.41/0.86, D7^{CD31Med}: 3.88/2.4525, D14^{CD31Hi}: 1.45/2.47, D14^{CD31Med}: 4.60/3.99, D28^{CD31Hi}: 2.16/2.65, D28^{CD31Med}: 14.53/15.63. The population of endothelial cells expressing CD31^{Hi} has been suggested as an anti-inflammatory reaction to stimuli [16, 36, 37], which is supported by the significant decreases in iNOS and CCL2 expression on D1 and D3, respectively. The proinflammatory population of CD31^{Med} was depleted until D14, which then returned to normal levels relative to control (Fig. 2A, Population %; Additional file 1: Fig. S1A). Although CD31^{Med} was reduced in number, an inflammatory phenotype was generated (Fig. 2B), with marked increases to VCAM-1, TNFα, and CCL2 on D1, an additional significant increase to ICAM-1 on D3, with a further increase to iNOS on D7. By D14, all markers except ICAM-1 reduced to normal levels relative to control. By D28, all markers measured returned to baseline expression levels. Taken together, these data indicate that a small population of endothelial cells could be responsible for the bulk of signaling and the proinflammatory response associated with our biomass exposure. However, a comprehensive panel of pro-inflammatory and anti-inflammatory markers would need to confirm. Regardless, endothelial cells are dynamically changing their phenotype following neuroimmune insult from woodsmoke inhalation.

Immune cell infiltration in the brain and resolution in response to woodsmoke

The observed increases in endothelial cell expression of adhesion molecules VCAM-1 and ICAM-1 (Fig. 2) indicate increased potential for immune cell adhesion and diapedesis across the blood–brain barrier. Therefore, these endothelial cell adhesion molecule results prompted a thorough investigation into whether activation of microglia or infiltration of peripheral immune cells subsequently occurred in the brain (Fig. 3). When examining microglial activation and peripheral immune infiltrates in the brain, which included neutrophils and nonspecific peripheral immune cell infiltration (Fig. 3), we utilized the following markers: activated microglia were distinguished from non-activated microglia based

Scieszka *et al. Journal of Neuroinflammation*   (2023) 20:192

Page 7 of 15

Table 1 *P* values calculated from flow cytometry results

		Day				
	Marker	**1**	**3**	**7**	**14**	**28**
CD31 High	Population	0.014	0.025	0.108	0.015	0.173
	TNF	0.673	0.373	0.077	0.197	0.344
	VCAM-1	0.481	0.865	0.500	0.357	0.337
	CCL2	0.181	0.040	0.102	0.448	0.965
	iNOS	0.022	0.158	0.125	0.301	0.396
CD31 Medium	Population	0.015	0.002	0.006	0.468	0.568
	TNF	0.060	0.003	0.000	0.157	0.948
	VCAM-1	0.043	0.002	0.001	0.415	0.150
	CCL2	0.019	0.003	0.000	0.552	0.348
	ICAM	0.078	0.010	0.009	0.021	0.723
	iNOS	0.103	0.158	0.048	0.328	0.834
Activated Microglia	Population	0.548	0.958	0.103	0.427	0.017
	TNF	0.595	0.066	0.036	0.043	0.018
	CD45	0.512	0.980	0.065	0.094	0.099
	iNOS	0.150	0.705	0.630	0.116	0.047
	Ly6C	0.854	0.657	0.094	0.013	0.185
Peripheral Immune Infiltrates	Population	0.013	0.222	0.104	0.042	0.227
	TNF	0.545	0.627	0.153	0.016	0.104
	CCL2	0.564	0.083	0.102	0.091	0.085
	CD45	0.931	0.166	0.040	0.028	0.138
	MHCII	0.462	0.209	0.106	0.037	0.035
Infiltrating Neutrophils	Population	0.501	0.328	0.448	0.046	0.041
	CD45	0.060	0.004	0.495	0.447	0.031
	Ly6C	0.023	0.079	0.448	0.300	0.004
	Ly6G	0.839	0.414	0.369	0.749	0.914
	MHCII	0.079	0.441	0.463	0.592	0.053

Yellow: trending increase/decrease. Green, significant difference

on combined expression levels of CD45 and CD11b [27]. Infiltrating neutrophils were identified based on their expression of the polymorphonuclear neutrophil (PMN) or neutrophil marker, Ly6G (1A8) [38]. The population of non-specific peripheral immune cells was identified as CD45 + cells that were Ly6G- (leukocytes that are not neutrophils).

This investigation revealed no statistically significant increase in the percentage of activated microglia until 28-day post-exposure. However, activated microglia increased expression of TNFα and CD45 beginning on D7, which persisted until D28 post-exposure (Fig. 3A, Table 1). Furthermore, increased expression of Ly6C and iNOS were observed on days 14 and 28,
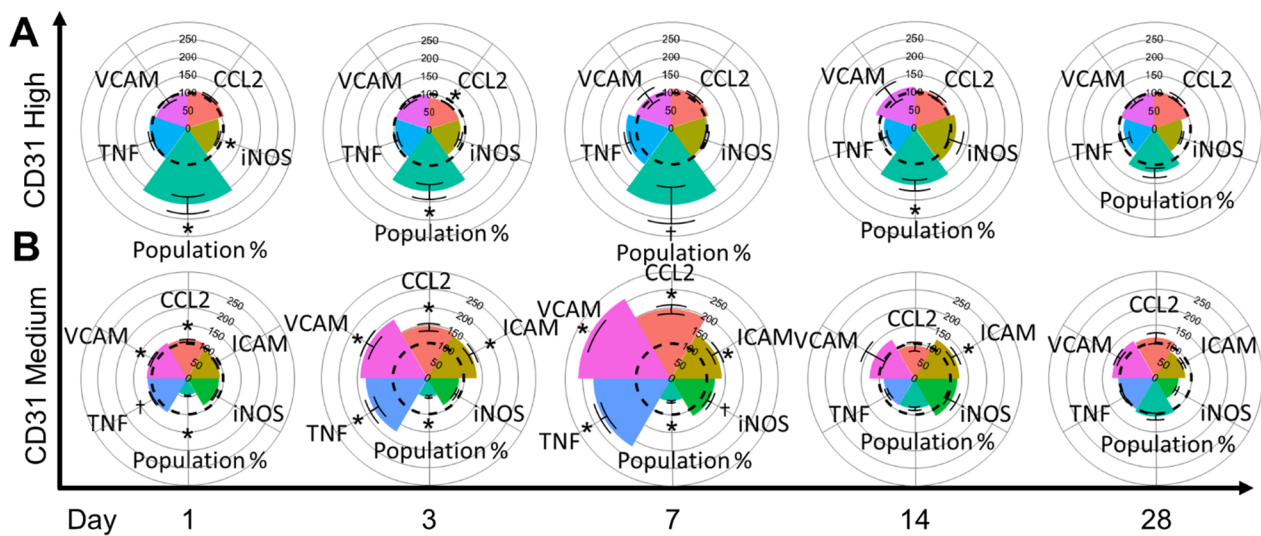
Fig. 2 Examining endothelial cell-specific responses by flow cytometry. **A, B** CD31 endothelial cells representing blood brain barrier; *y*-axis: marker grouping; *x*-axis: day post-exposure; colored radar plot slice: marker of interest measured; dotted line: 100% baseline control; all values normalized to filtered air (FA) controls. **A** Anti-inflammatory CD31^{Hi} cells showed an immediate increase in population percent and a decrease in iNOS (day 1). On day 3, population percent remained significantly increased coinciding with a reduction in CCL2 expression. Population percent trended higher on day 7 and was significantly higher on day 14. **B** Proinflammatory CD31^{Med} saw a decreased population percent, but increased TNFα, VCAM-1, and CCL2 expression through days 1–7. ICAM expression increased on day 3 and remained up until day 14

respectively. When examining non-specific peripheral immune infiltrates (Fig. 3B, Table 1), we observed trending increases to the peripheral immune infiltrate population percent beginning on D7, which coincided with increased expression of MHCII, CCL2, and CD45. All markers were either significantly increased or trending on D14, with MHCII significantly increased on D28, along with trending increases to CCL2 and TNFα. When examining neutrophil infiltration (Fig. 3C), we observed reduced expression on D1 of CD45, Ly6C and MHCII, with CD45 remaining depressed on D3. On D14, a significant population increase was observed. Interestingly, D28 post-exposure saw a significant reduction in population percent, coinciding with an increase in CD45, Ly6C, and MHCII. These data largely show an initial reduction in neutrophils after exposure, a neutrophil population increase on D14, with subsequent neutrophil exclusion on 28. However, the neutrophils remaining within the hippocampus on D28 appeared to be highly inflammatory with significantly elevated CD45, Ly6C, and MHCII. Taken together, these data indicated a long-term (at least 28 days) microglial response, a D14 neutrophil and non-specific peripheral immune infiltration, with a small, but potent inflammatory neutrophil population still present on D28 (Additional file 1: Fig. S1).

Metabolomic changes in the brain following wood smoke exposure

The dynamic neurocellular alterations following woodsmoke inhalation (Additional file 1: Fig. S1A) prompted an investigation into small molecule changes in the hippocampal region. We utilized both an untargeted metabolomic panel and a panel targeted to NAD$^+$ synthesis pathways. Broadly, the targeted NAD$^+$ panel was utilized based on our group's previous work showing woodsmoke-induced decreases in neuroprotective metabolites and decreases to NAD$^+$, itself [6].

Regarding the untargeted panel, initial heatmapping revealed consistent visual patterns that persisted over the 28-day time course (Fig. 4A). This method utilized a limma-based linear modeling to show 113 total significantly altered metabolites (Additional file 1: Table S1). However, we sought to determine whether consistencies arose in the altered metabolites. Thus, we utilized a Venn diagram to illustrate significantly altered metabolites that overlapped per day (Fig. 4B). These data showed only minor overlaps, initially indicating temporal compensation mechanisms of stimuli and response. Broadly, D1 showed the largest overlap with each subsequent day (D3 = 13, D7 = 17, D14 = 14, and D28 = 40 metabolites). However, we reasoned the sheer number of statistically significant metabolites from D1 could be casting the widest net to overlap other days. From this, we employed Jaccard calculations that reduce numerical weight bias (Fig. 4C). Regardless of methodology
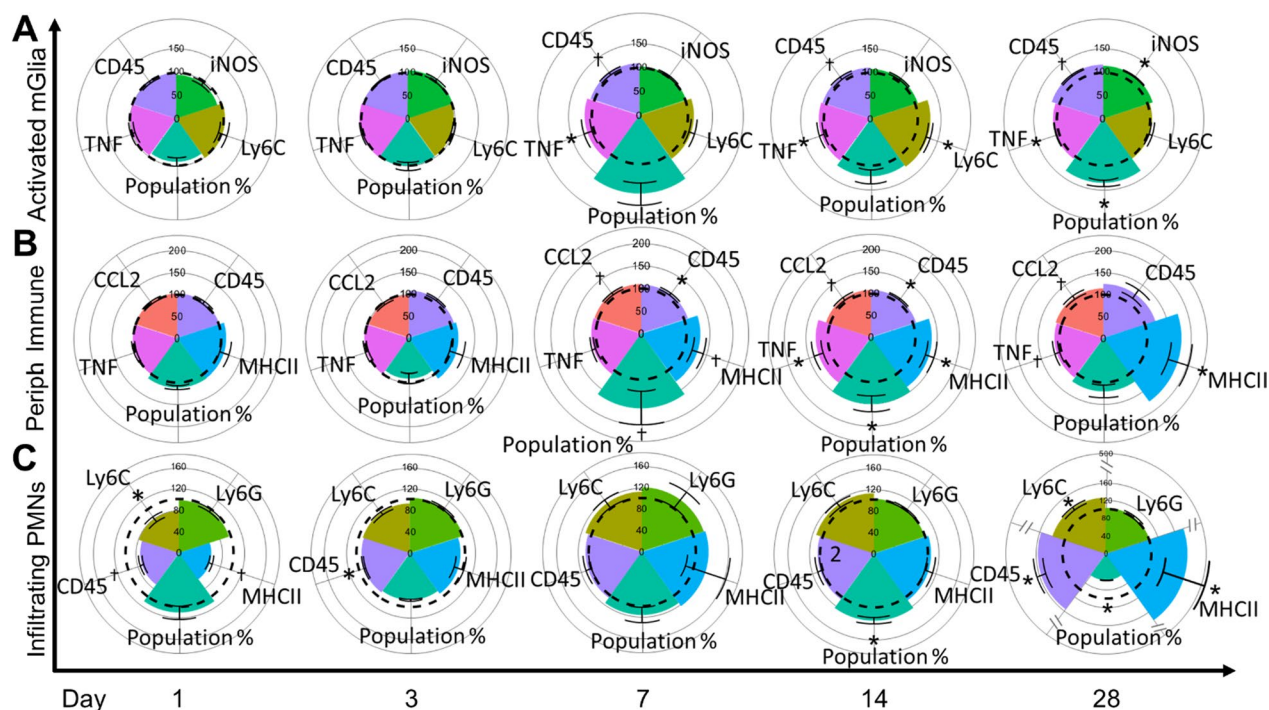
Scieszka *et al. Journal of Neuroinflammation*   (2023) 20:192

Page 9 of 15

Fig. 3 Microglial activation and peripheral immune infiltration. **A–C** *y*-axis: cell subset grouping; *x*-axis: day post-exposure; colored radar plot slice: marker of interest measured; dotted line: 100% baseline control; all values normalized to filtered air (FA) controls. **A** Activated microglial population increased on day 28. TNFα increased on day 7 and remained increased on day 28. CD45 trended upward starting on day 7 through day 28. iNOS expression increased on day 28. **B** Nonspecific peripheral immune infiltration population percent trended upward on day 7, showed significant increases on day 14, and was resolved by day 28. TNFα expression increased on day 14 and trended upward on day 28. CCL2 expression trended upward starting on day 7 and remained trending upward on day 28. CD45 expression increased on days 7 and 14 but was resolved by day 28. MHCII trended upward on day 7 and showed significant increases on days 14–28. **C** Infiltrating polymorphonuclear neutrophils (PMNs) showed a reduction in Ly6C on day 1 with a trending decrease to MHCII. CD45 trended downward on day 1 and was significantly reduced on day 3. On day 14, population percent increased. On day 28, population percent decreased, but CD45, Ly6C, and MHCII showed significant increases. *$p < 0.05$, †$p < 0.10$

employed, we see the strongest correlation between days 1 and 28 (J-index = 0.1266). Interestingly, these data showed a strong initial hippocampal impact of 241 significantly altered metabolites on D1, rapid compensation and decrease to a mere 35 significant metabolites on D3, with a gradual ramping up of 47 metabolites on D7, 69 on D14, and increasing to 115 significantly altered metabolites on D28 (Additional file 1: Fig. S1). These data mirror the dynamic pattern seen in the cell populations. Namely, a large initial response was also seen in the endothelial phenotype, while peripheral immune infiltration began subsequently, resulting in an inflammatory response that was not fully resolved by D28. The global metabolomic effect may be influenced by the specific and complex cellular responses resulting from activation and suppression of cell populations, such as the endothelium, resident neuro-immune cells, different neuronal subtypes, and infiltrating peripheral immune cells. More specifically, the endothelial response on D1 appears to cause the greatest shift in significantly altered metabolites, while

the gradual increase of immune responses caused a gradual increase in significantly altered metabolites.

To examine individual metabolites affected, we overlapped volcano plots for each day (Fig. 4D). On D1, we observed an increase to α-aminoadipic acid, which has been implicated as an inhibitory regulator of kynurenic acid synthesis in the hippocampus [39]. In addition, we observed a decrease to arginine–glutamine (arg–gln), and a potential compensation mechanism in the D3 increase to oxoproline—a facilitator of amino acid transport across the BBB [40]. Of note, we observed a reduction in the 5α-Pregnane-3,20-dione (5α-Dihydroprogesterone; 5α-DHP), and a D7 decreased abundance of the dipeptides arg–gln and asn–arg (asparagine–arginine). In addition, we observed an increased level of N-acetyl-L-aspartic acid (NAA), which is known to have a positive impact on working memory [41]; perhaps a compensation mechanism from downregulated metabolites seen on days 1–3. On D28, notable observations included a decrease in 3-methoxytyramine (3-MT) and glutaurine.
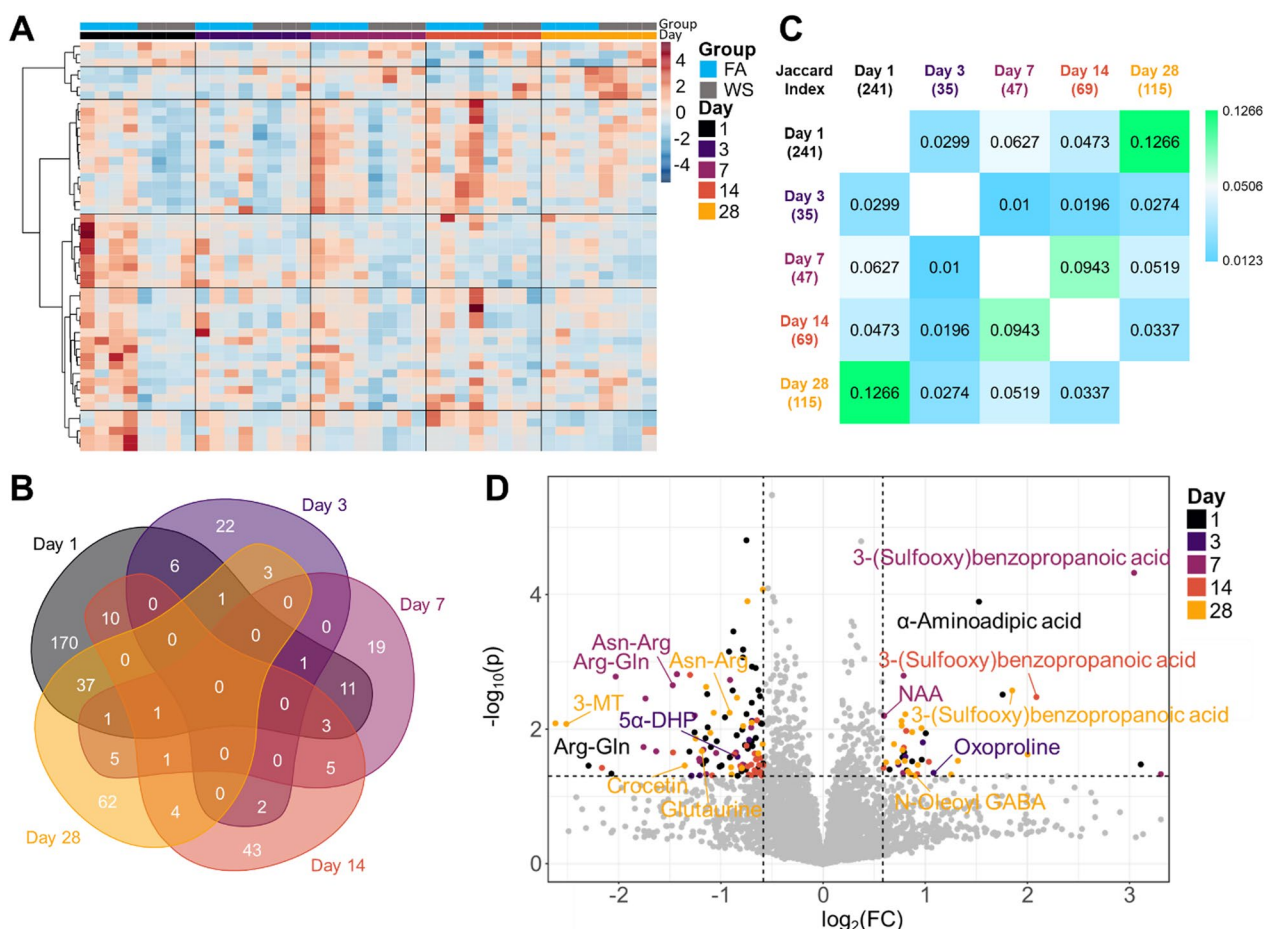
Fig. 4 Untargeted metabolomic temporal analysis. **A** Heatmap of top 50 significant metabolites. Limma-based linear modeling, Pearson distance, Ward clustering. **B** Venn diagram of statistically significant metabolites per day. Day 1 has the strongest overlapping signature with each subsequent day. Overlap by day is as follows, D1:D3 = 13, D1:D7 = 17, D1:D14 = 14, D1:D28 = 40, D3:D7 = 1, D3:D14 = 2, D3:D28 = 4, D7:D14 = 10, D7:D28 = 8, D14:D28 = 6. **C** Jaccard index correction for multiple statistically significant metabolites. Day 1 has the strongest overlap with day 28 (j-index = 0.1266), while days 7 and 14 have the strongest overlap with each other (j-index = 0.0943). **B**, **C** Data normalized by quality control, unlogged, student's *t* test. **D** Volcano plot overlay from each day. *Arg* Arginine, *Asn* Asparagine, *DHP* Dihydroprogesterone, *Gln* glutamine, *MT* Methoxytyramine, *NAA* N-acetyl-L-aspartic acid, *FC* fold-change, *p*: *p* value. Data normalized by quality control samples and $\log_2()$

Taken together, these data potentially indicate a consistent reduction in amino acid dipeptides over time and suggest mood alterations.

From the NAD^+ panel, initial heatmapping revealed less consistent patterns than the untargeted panel (Fig. 5A). Furthermore, only 2 woodsmoke-responsive metabolites were deemed significant in the exposed group after limma-based linear modeling (NADH and Indole, data not shown) resulting in the variance-based interquartile range being represented (Fig. 5A). Through similar volcano plot overlaying as in Fig. 3D, we overlayed all days of our NAD^+ panel on a single plot (Fig. 5A). Largely, D1 revealed that NAD^+ and Nicotinic acid adenine dinucleotide (NaAD) abundances were increased, with decreased abundance seen in glutamate, indole, niacin,

and N'-Formylkynurenine. Although no metabolites appeared significantly altered by woodsmoke between D3–D14, D28 metabolites of NAD^+ and NADH showed decreased abundance. After removing outliers, we plotted graphs on the Preiss–Handler and salvage pathways to examine specific points of interest for future investigation (Fig. 5C). Quinolinic acid and niacin were immediately decreased on D1, but slowly recovered and overshot baseline levels on D28. Nicotinic acid adenine dinucleotide (NaAD) and NAD^+ levels followed an opposite pattern of increased abundance on D1 followed by eventual deficits on D28. The precursor nicotinamide mononucleotide exhibited no such trend, nor did the post-cursors nicotinamide or ADP ribose. Taken together, these data indicate trends for the hippocampus that persist for the
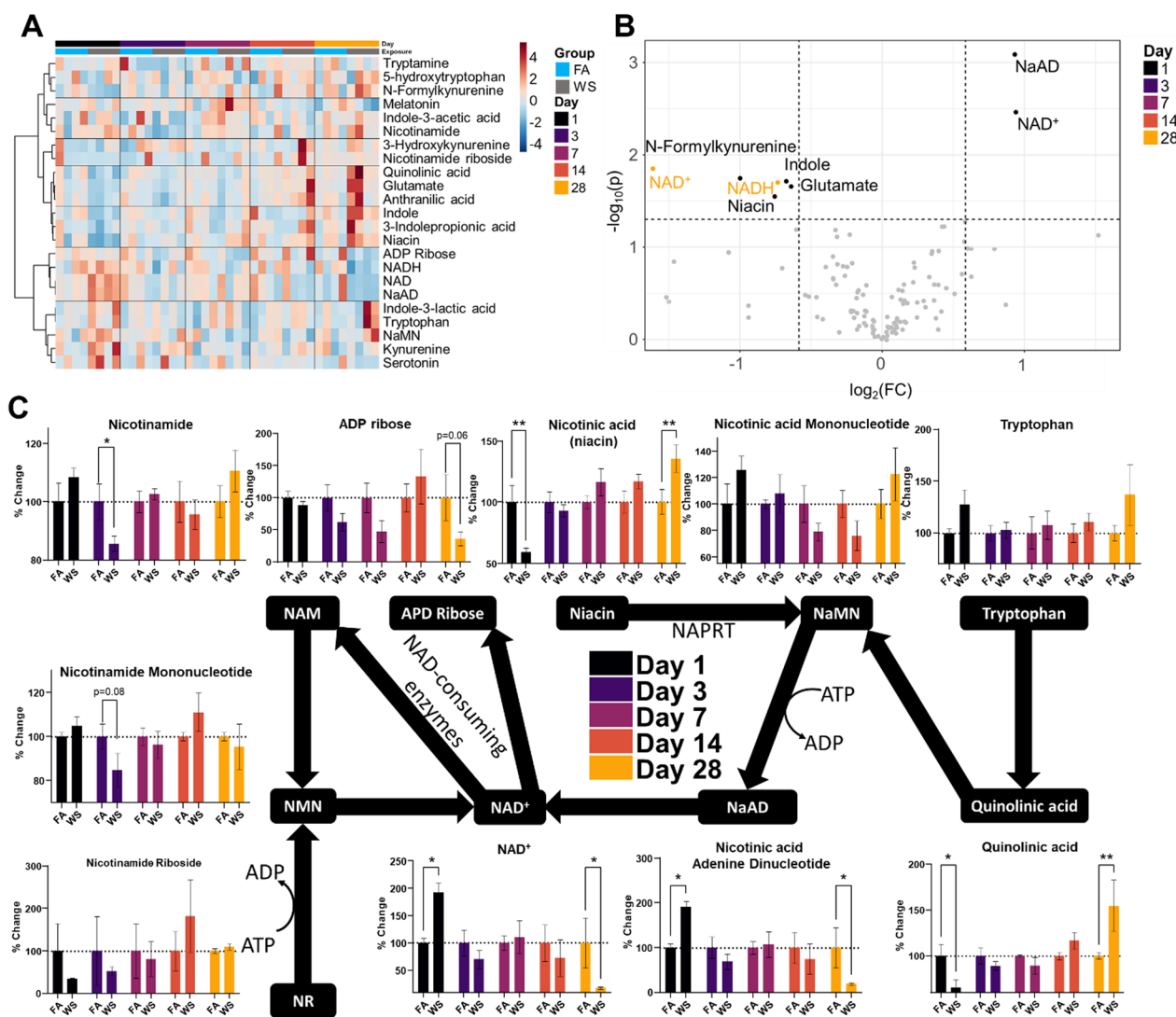
Fig. 5 Targeted NAD$^+$ metabolomic temporal analysis. **A** Heatmap of all metabolites within the panel. Interquartile range variance shown, Pearson distance, Ward clustering. **B** Volcano plot overlay from each day. *NaAD* Nicotinic acid Adenine Dinucleotide, *NAD* Nicotinamide Adenine Dinucleotide, *NADH* Nicotinamide Adenine Dinucleotide + Hydrogen. Data normalized by quality control samples, log$_2$() transformed. **C** Preiss–Handler and salvage pathways with accompanying temporal bar charts. Data normalized by quality control samples, log$_2$() transformed and outliers removed

duration of our 28-day time course. Furthermore, the NAD$^+$ depletion is particularly unsettling and warrants further investigation as the precursors and post-cursors do not indicate the reason for abundance and depletion seen in this study.

Discussion

Summarily, these data indicate that the neuroinflammatory and neurometabolomic alterations following woodsmoke exposure can persist up to and possibly longer than 28 days. The neuroinflammation driven by woodsmoke was consistent with that observed after

a real-world exposure to PM in New Mexico that was largely derived from California wildfires [6]. In the present study, fresh biomass combustion emissions were used, at a 24 h average concentration that fits within real-world exposure (44 vs ~ 35–190 µg/m^3) [42]. The observation of a prolonged period of neuroinflammation and hippocampal metabolic alterations out to 28 days after the end of exposures aligns with epidemiological findings of persistent deficits in cognition and attention in woodsmoke-exposed populations [7], as well as prolonged post-traumatic stress and depression that accompany severe wildfire events [43–46].

Scieszka *et al. Journal of Neuroinflammation* (2023) 20:192

Page 12 of 15

Neurovascular endothelial cells exhibited a response to woodsmoke that included both inflammatory and anti-inflammatory components. Following 2 weeks of intermittent exposure, mice showed a robust increase in the CD31^{Hi} endothelial cells that exhibited reduced relative expression of inflammatory markers (CCL2, iNOS). We observed a reduced population of CD31^{Med} endothelial cells associated with promoting the neuroinflammatory response to woodsmoke, but these cells exhibited increased expression of VCAM-1, ICAM-1, CCL2, TNFα, and iNOS to varying degrees even 14 days after the exposures had ended. Both pro- and anti-inflammatory endothelial cell responses had largely subsided by day 28. Current understanding points to a reduced endothelial expression of CD31 in Alzheimer's disease compared to healthy individuals and decreased expression in arterial beds relative to venous and capillary [47]. Accelerating recovery of inflammation may have value for neurological health, in which case both populations of anti-inflammatory and proinflammatory endothelial cells represent interesting therapeutic targets after woodsmoke exposure.

Interestingly, the activated microglial response to woodsmoke increased on D7, continuing through D28. Activated microglia can release quinolinic acid, and our metabolomic results show a gradual increasing concentration of quinolinic acid until statistical significance is achieved on D28. If this response lasts, neurological damage could occur due to quinolinic acid having the potential for excitotoxic effects. Here, we reported a population of activated microglia expressing Ly6C on D14. However, there is evidence that these could be microglial precursors being differentiated and recruited to fight ongoing infections/stimuli [20]. If true, this would represent a first-wave elimination of microglia, perhaps after undergoing apoptosis or through other elimination pathways. These would necessarily need to be replaced through the differentiation of microglial precursors and recruited to the site of ongoing response(s). The subsequent D28 increase to activated microglia population percent could be confirming the current literature and the hypothesis of first-wave elimination followed by subsequent reinforcements posited here.

We also observed a D14 neutrophil and non-specific peripheral immune invasion. On this point, there are two current schools of thought, with one postulate that the inhaled particles are able to escape the lungs and enter the circulation [48, 49]. Upon reaching the BBB, the peripheral immune system is notified and recruited for a response to the inhaled particles. Another school of thought is that the inhaled particles cause a localized response in the lung, and the fragmented response peptides escape into the circulation from the lungs [13, 50, 51]. When the fragmented lung response peptides reach the BBB, the peripheral immune system is notified and recruited for a response to the self-peptides. Although the molecule/particle causing the recruitment will change based on the theory, the end result for immune recruitment holds based on our peripheral immune response. This conclusion is also strengthened based on the constant and large number of neutrophils in circulation [38, 52]. In addition, ozone inhalation can activate microglia and cause BBB decrements [10, 26], despite being so reactive that it is unable to penetrate further than 0.1 μm in the epithelial fluid lining of the lung [53, 54]. A final thought regarding neutrophils, the remaining neutrophil population on D28 was significantly lower than FA controls but appeared to be responding strongly to a stimulus. Conceivably this could reflect a penetrance of particulates into the brain and an immunological process for removal.

Hippocampal metabolite changes may reaffirm recent observations of reduced learning and attention after wildfire exposure, using an app-based experiment performed in humans [7]. This conclusion is based on our observed reductions in glutamate, glutaurine, 3-MT, 5α-DHP, NAD$^+$, and the decreased ratio of NAD$^+$/NADH. 5α-DHP is a neuroprotective [55] agonist for the GABA$_A$ receptor that is synthesized from progesterone and reductions have been linked to social isolation and depression [56]. 5α-DHP has high affinity for the progesterone receptor (which are found in the hippocampus) and regulates DNA transcription [56]. 3-MT is a dopamine metabolite implicated in movement control [57], while glutaurine naturally mimics the effects of valium [58]. Broadly, we observed the strongest metabolic response on D1, with an immediate reduction in response by D3, and a progressive return to strong response by D28 (Figs. 4B, D, B, Additional file 1: Fig. S1B). These data largely agree with the flow cytometry results that indicate a delayed peripheral immune response and microglial activation persisting through D28. Our intent for this study was to reveal the time course for resolution of the neurological effects of woodsmoke exposure; 28 days was seemingly insufficient in this mouse model.

Through the untargeted panel, we observed an increase in α-Aminoadipic acid on D1 (Fig. 4D), which has been shown to downregulate kynurenic acid [39]. This increase coincided with decreases in quinolinic acid and N'-Formylkynurenine abundances seen in our NAD$^+$ panel (Fig. 5B, C). Together, these could indicate that the kynurenine and tryptophan pathways were shifted toward NAD$^+$ production, rather than production of kynurenic acid and quinolinic acid [59]. This is based on α-aminoadipic acid downregulating kynurenic acid, which implicates the shift toward quinolinic acid and

NAD$^+$ production. This is further corroborated by the D1 decrease in niacin (Fig. 5C) and increased NAD$^+$ abundance (Fig. 5C). Quinolinic acid can be excitotoxic with persistent exposure through activated microglia [60]. However, kynurenic acid is released from astrocytes and promotes neuronal stability [61, 62]. The increased abundance of α-aminoadipic acid and reductions downregulation of kynurenic acid, along with reductions in 3-MT and 5α-DHP may contribute to the epidemiological findings of persistent deficits in cognition, attention and mood alterations observed following woodsmoke exposure [56, 57].

Additional interesting and confounding points related to hippocampal metabolite changes include the consistent reductions in amino acid dipeptides over time and increases to 3-(sulfooxy)benzenepropanoic acid. We are yet unclear as to the meaning, which warrants further investigation. In addition, we observed a decrease to the dipeptide arginine–glutamine (Arg–Gln), which is formed from L-arginine and L-glutamine residues. On D3, we observed a potential compensation mechanism for reduced Arg–Gln through an increased oxoproline. This metabolite has been shown to facilitate amino acid transport across the blood brain barrier [40]. Finally, D28 crocetin was decreased and has been shown to protect against beta-amyloid brain abundance [63]. In addition, 3-O-beta-D-galactosyl-sn-glycerol abundance was decreased, whose biosynthesis have been observed in mouse brain microsomes [64], with implications in anti-inflammatory potential [65]. The observed increase to N-Oleoyl GABA will mimic GABA effects and reduce neuronal excitability and inhibition of neurotransmission. Curiously, 3-(sulfooxy)benzenepropanoic acid was observed to be increased on D7, D14, and D28; however, the neurological functions are unknown and the proposed source is food consumption. Yet, the mouse weights did not statistically deviate from FA controls throughout the course of experiments (Additional file 1: Fig. S1).

Regarding the NAD$^+$ panel, the decreased abundance at D28 may imply increased demand from NAD$^+$ consuming enzymes or pathways. Although we were unable to determine which enzyme or pathway was consuming the NAD$^+$, these data do corroborate previous studies that show a decrease in NAD$^+$ abundance after wildfire smoke exposure [6]. There are many important NAD$^+$ consuming enzymes within the brain parenchyma, including sirtuins and poly(ADP-ribose) polymerases. Without these molecules—and coupled with the highly responsive neutrophil data on D28—there exists increased potential for damage and inflammatory persistence. Furthermore, if the model of fragmented peptides reaching the BBB is correct, then these neutrophils are potentially reacting to self. This has much broader implications, given that wildfire acres burned yearly have roughly doubled since 1985 and the steadily increasing incidence of autoimmunity based on epidemiological evidence [1, 66].

Caveats to this study include a limited study design related to fuel source, timing of exposures, mouse model (age and sex), duration of examined timepoints, and observational outcomes. There are a multitude of organic and non-organic fuel sources for wildfires, including brush, grasses, leaves, cars, paint, asbestos, plastics, and others. In addition, our exposure paradigm emphasized replicability at the partial expense of real-world parameters. Our exposure levels were quite modest compared to some wildfires, including reported exposures in Washington State from 2020, where it was estimated that 7.1 million people were exposed to average daily particulate matter concentrations ranging from 30 to 190 μg/m^3 for 13 consecutive days [42]. We chose an intermittent exposure scenario, however, as during wildfire events, the ambient particulate matter concentration can fluctuate significantly between days, or even hours as prevailing winds change direction. Finally, the descriptive nature and timepoints utilized did not allow for a full resolution of immune inflammation, nor did we explore behavioral or histopathological impacts of the major findings.

Summarily, the major findings of this study include the duration of resolution, impacts on inflammatory and metabolite profiles, and corroboration with recent human exposure data. The duration of endothelial neuroimmune activity and resolution appeared to be resolved within 7–14 days. However, microglial activation, peripheral immune infiltration, and neutrophil invasion began during endothelial response and lasted until our final timepoint examined (Additional file 1: Fig. S1C). Metabolomic profiles saw the largest effect on D1, which is likely to be associated with endothelial response. This decreased by day 3 but gradually ramped up to nearly half the original response by day 28, which is likely to be associated with the immune cell response. Future studies could employ vulnerable models to delineate this endothelial cell-specific response vs immune response and increase resolution of neuroimmune vs metabolomic changes per cell type to understand the relationships. Finally, implied behavioral, cognitive, and mood alterations could be revisited to determine mechanistic alterations and confirm observational results.

Scieszka *et al. Journal of Neuroinflammation*   (2023) 20:192

Page 14 of 15

Supplementary Information

The online version contains supplementary material available at https://doi.org/10.1186/s12974-023-02874-y.

Additional file 1: Table S1. List of all metabolites affected from limma-based linear modelling. **Fig. S1.** Neuroinflammatory and Metabolomic Temporal Dynamics.

Declarations

Ethics approval and consent to participate
All studies were conducted with the approval and oversight of a registered IACUC institute on verified protocols according to the highest standards.

Competing interests
The authors state that they have no competing interests.

Author details
[1]Department of Pharmaceutical Sciences College of Pharmacy, University of New Mexico, MSC09 5360; 1, Albuquerque, NM 87131-0001, USA. [2]Florida International University Center for Translational Sciences, Port St. Lucie, FL 34987, USA. [3]Department of Molecular Genetics and Microbiology, Department of Neurology, School of Medicine, University of New Mexico, Albuquerque, NM 87131, USA. [4]Department of Pathology, School of Medicine, University of New Mexico Health Sciences Center, Albuquerque, NM 87131, USA. [5]Department of Biochemistry and Molecular Biology, School of Medicine, University of New Mexico Health Sciences Center, Albuquerque, NM 87131, USA. [6]Department of Pharmacy Practice and Administrative Sciences, College of Pharmacy, University of New Mexico, Albuquerque, NM 87131, USA.

References
1. Wildfires and Acres | National Interagency Fire Center [Internet]. https://www.nifc.gov/fire-information/statistics/wildfires. Accessed 13 Jan 2023.
2. Adetona O, Reinhardt TE, Domitrovich J, Broyles G, Adetona AM, Kleinman MT, et al. Review of the health effects of wildland fire smoke on wildland firefighters and the public. Inhal Toxicol. 2016;28:95–139.
3. Reid CE, Brauer M, Johnston FH, Jerrett M, Balmes JR, Elliott CT. Critical review of health impacts of wildfire smoke exposure. Environ Health Perspect. 2016;124:1334–43.
4. Jaiswal S, Jalbert I, Schmid K, Tein N, Wang S, Golebiowski B. Smoke and the eyes: a review of the harmful effects of wildfire smoke and air pollution on the ocular surface. Environ Pollut Barking Essex. 1987;2022(309):119732.
5. Mirabelli MC, Künzli N, Avol E, Gilliland FD, Gauderman WJ, McConnell R, et al. Respiratory symptoms following wildfire smoke exposure: airway size as a susceptibility factor. Epidemiol Camb Mass. 2009;20:451–9.
6. Scieszka D, Hunter R, Begay J, Bitsui M, Lin Y, Galewsky J, et al. Neuroinflammatory and neurometabolomic consequences from inhaled wildfire smoke-derived particulate matter in the Western United States. Toxicol Sci Off J Soc Toxicol. 2022;186:149–62.
7. Cleland SE, Wyatt LH, Wei L, Paul N, Serre ML, West JJ, et al. Short-term exposure to wildfire smoke and PM2.5 and cognitive performance in a brain-training game: a longitudinal study of U.S. adults. Environ Health Perspect. 2022;130:67005.
8. Levesque S, Surace MJ, McDonald J, Block ML. Air pollution & the brain: subchronic diesel exhaust exposure causes neuroinflammation and elevates early markers of neurodegenerative disease. J Neuroinflammation. 2011;8:105.
9. Levesque S, Taetzsch T, Lull ME, Kodavanti U, Stadler K, Wagner A, et al. Diesel exhaust activates and primes microglia: air pollution, neuroinflammation, and regulation of dopaminergic neurotoxicity. Environ Health Perspect. 2011;119:1149–55.
10. Mumaw CL, Levesque S, McGraw C, Robertson S, Lucas S, Stafflinger JE, et al. Microglial priming through the lung-brain axis: the role of air pollution-induced circulating factors. FASEB J Off Publ Fed Am Soc Exp Biol. 2016;30:1880–91.
11. Block ML, Kodavanti UP. The use of standardized diesel exhaust particles in Alzheimer's disease research. J Alzheimers Dis JAD. 2021;84:607–8.
12. Aragon MJ, Topper L, Tyler CR, Sanchez B, Zychowski K, Young T, et al. Serum-borne bioactivity caused by pulmonary multiwalled carbon nanotubes induces neuroinflammation via blood-brain barrier impairment. Proc Natl Acad Sci U S A. 2017;114:E1968–76.
13. Mostovenko E, Young T, Muldoon PP, Bishop L, Canal CG, Vucetic A, et al. Nanoparticle exposure driven circulating bioactive peptidome causes systemic inflammation and vascular dysfunction. Part Fibre Toxicol. 2019;16:20.
14. Mostovenko E, Saunders S, Muldoon PP, Bishop L, Campen MJ, Erdely A, et al. Carbon nanotube exposure triggers a cerebral peptidomic response: barrier compromise, neuroinflammation, and a hyperexcited state. Toxicol Sci Off J Soc Toxicol. 2021;182:107–19.
15. Mostovenko E, Canal CG, Cho M, Sharma K, Erdely A, Campen MJ, et al. Indirect mediators of systemic health outcomes following nanoparticle inhalation exposure. Pharmacol Ther. 2022;235: 108120.
16. Woodfin A, Voisin M-B, Nourshargh S. PECAM-1: a multi-functional molecule in inflammation and vascular biology. Arterioscler Thromb Vasc Biol. 2007;27:2514–23.
17. Privratsky JR, Tourdot BE, Newman DK, Newman PJ. The anti-inflammatory actions of platelet endothelial cell adhesion molecule-1 do not involve regulation of endothelial cell NF-kappa B. J Immunol Baltim Md. 1950;2010(184):3157–63.
18. Gschwandtner M, Derler R, Midwood KS. More than just attractive: how ccl2 influences myeloid cell behavior beyond chemotaxis. Front Immunol. 2019;10:2759.
19. Greiner T, Kipp M. What guides peripheral immune cells into the central nervous system? Cells. 2021;10:2041.
20. Getts DR, Terry RL, Getts MT, Müller M, Rana S, Shrestha B, et al. Ly6c+ "inflammatory monocytes" are microglial precursors recruited in a pathogenic manner in West Nile virus encephalitis. J Exp Med. 2008;205:2319–37.
21. Doran SJ, Ritzel RM, Glaser EP, Henry RJ, Faden AI, Loane DJ. Sex differences in acute neuroinflammation after experimental traumatic brain injury are mediated by infiltrating myeloid cells. J Neurotrauma. 2019;36:1040–53.
22. Han J, Fan Y, Zhou K, Blomgren K, Harris RA. Uncovering sex differences of rodent microglia. J Neuroinflammation. 2021;18:74.
23. Beery AK, Zucker I. Sex bias in neuroscience and biomedical research. Neurosci Biobehav Rev. 2011;35:565–72.
24. Mogil JS, Chanda ML. The case for the inclusion of female subjects in basic science studies of pain. Pain. 2005;117:1.
25. Kim YH, Warren SH, Krantz QT, King C, Jaskot R, Preston WT, et al. Mutagenicity and lung toxicity of smoldering vs. flaming emissions from various biomass fuels: implications for health effects from wildland fires. Environ Health Perspect. 2018;126:017011.
26. Tyler CR, Noor S, Young TL, Rivero V, Sanchez B, Lucas S, et al. Aging exacerbates neuroinflammatory outcomes induced by acute ozone exposure. Toxicol Sci Off J Soc Toxicol. 2018;163:123–39.
27. Brandenburg S, Blank A, Bungert AD, Vajkoczy P. Distinction of microglia and macrophages in glioblastoma: close relatives, different tasks? Int J Mol Sci. 2021;22:194.
28. Qi Y, Gu H, Song Y, Dong X, Liu A, Lou Z, et al. Metabolomics study of resina draconis on myocardial ischemia rats using ultraperformance

Scieszka *et al. Journal of Neuroinflammation*   (2023) 20:192

Page 15 of 15

liquid chromatography/quadrupole time-of-flight mass spectrometry combined with pattern recognition methods and metabolic pathway analysis. Evid-Based Complement Altern Med. 2013;2013: 438680.

29. Yao W, Gu H, Zhu J, Barding G, Cheng H, Bao B, et al. Integrated plasma and urine metabolomics coupled with HPLC/QTOF-MS and chemometric analysis on potential biomarkers in liver injury and hepatoprotective effects of Er-Zhi-Wan. Anal Bioanal Chem. 2014;406:7367–78.

30. Wei Y, Jasbi P, Shi X, Turner C, Hrovat J, Liu L, et al. Early breast cancer detection using untargeted and targeted metabolomics. J Proteome Res. 2021;20:3124–33.

31. Gu H, Zhang P, Zhu J, Raftery D. Globally optimized targeted mass spectrometry: reliable metabolomics analysis with broad coverage. Anal Chem. 2015;87:12355–62.

32. MetaboAnalyst [Internet]. https://www.metaboanalyst.ca/. Accessed 26 May 2023.

33. Pang Z, Chong J, Li S, Xia J. MetaboAnalystR 3.0: toward an optimized workflow for global metabolomics. Metabolites. 2020;10:186.

34. Compare lists-multiple list comparator-Venn diagram generator, free online tool to find set intersections. https://molbiotools.com/listcompare.php. Accessed 13 Jan 2023.

35. Ritchie ME, Phipson B, Wu D, Hu Y, Law CW, Shi W, et al. Limma powers differential expression analyses for RNA-sequencing and microarray studies. Nucleic Acids Res. 2015;43: e47.

36. PECAM-1: Conflicts of Interest in Inflammation - PMC [Internet]. https://www.ncbi.nlm.nih.gov/pmc/articles/PMC2917326/. Accessed 1 Feb 2023.

37. Endothelial functions of PECAM-1 (CD31)-PMC [Internet]. https://www.ncbi.nlm.nih.gov/pmc/articles/PMC4986701/. Accessed 1 Feb 2023.

38. Rosales C. Neutrophil: a cell with many roles in inflammation or several cell types? Front Physiol. 2018;9:113.

39. L-alpha-aminoadipic acid as a regulator of kynurenic acid production in the hippocampus: a microdialysis study in freely moving rats - PubMed [Internet]. https://pubmed.ncbi.nlm.nih.gov/8566117/. Accessed 1 Feb 2023.

40. Lee WJ, Hawkins RA, Peterson DR, Viña JR. Role of oxoproline in the regulation of neutral amino acid transport across the blood-brain barrier. J Biol Chem. 1996;271:19129–33.

41. Neuroscience. https://doi.org/10.1080/00207594.2012.709117

42. Liu Y, Austin E, Xiang J, Gould T, Larson T, Seto E. Health Impact Assessment of PM2.5 attributable mortality from the September 2020 Washington State Wildfire Smoke Episode. MedRxiv Prepr Serv Health Sci. 2020;2020.09.19.20197921.

43. Mao W, Adu M, Eboreime E, Shalaby R, Nkire N, Agyapong B, et al. Post-traumatic stress disorder, major depressive disorder, and wildfires: a fifth-year postdisaster evaluation among residents of Fort Mcmurray. Int J Environ Res Public Health. 2022;19:9759.

44. Hong JS, Hyun SY, Lee JH, Sim M. Mental health effects of the Gangwon wildfires. BMC Public Health. 2022;22:1183.

45. Berger W, Coutinho ESF, Figueira I, Marques-Portella C, Luz MP, Neylan TC, et al. Rescuers at risk: a systematic review and meta-regression analysis of the worldwide current prevalence and correlates of PTSD in rescue workers. Soc Psychiatry Psychiatr Epidemiol. 2012;47:1001–11.

46. Wagner SL, White N, Randall C, Regehr C, White M, Alden LE, et al. Mental disorders in firefighters following large-scale disaster. Disaster Med Public Health Prep. 2021;15:504–17.

47. Yang AC, Vest RT, Kern F, Lee DP, Agam M, Maat CA, et al. A human brain vascular atlas reveals diverse mediators of Alzheimer's risk. Nature. 2022;603:885–92.

48. Nemmar A, Hoet P, Vanquickenborne B, Dinsdale D, Thomeer M, Hoylaerts M, et al. Passage of inhaled particles into the blood circulation in humans. Circulation. 2002;105:411–4.

49. Qi Y, Wei S, Xin T, Huang C, Pu Y, Ma J, et al. Passage of exogenous fine particles from the lung into the brain in humans and animals. Proc Natl Acad Sci U S A. 2022;119: e2117083119.

50. Pemberton CJ, Siriwardena M, Kleffmann T, Richards AM. C-type natriuretic peptide (CNP) signal peptide fragments are present in the human circulation. Biochem Biophys Res Commun. 2014;449:301–6.

51. Foo JYY, Wan Y, Schulz BL, Kostner K, Atherton J, Cooper-White J, et al. Circulating fragments of N-terminal pro-B-type natriuretic peptides in plasma of heart failure patients. Clin Chem. 2013;59:1523–31.

52. Summers C, Rankin SM, Condliffe AM, Singh N, Peters AM, Chilvers ER. Neutrophil kinetics in health and disease. Trends Immunol. 2010;31:318–24.

53. Pryor WA, Squadrito GL, Friedman M. A new mechanism for the toxicity of ozone. Toxicol Lett. 1995;82–83:287–93.

54. Postlethwait EM, Cueto R, Velsor LW, Pryor WA. O3-induced formation of bioactive lipids: estimated surface concentrations and lining layer effects. Am J Physiol. 1998;274:L1006-1016.

55. Nguyen PN, Billiards SS, Walker DW, Hirst JJ. Changes in 5alpha-pregnane steroids and neurosteroidogenic enzyme expression in the perinatal sheep. Pediatr Res. 2003;53:956–64.

56. Dong E, Matsumoto K, Uzunova V, Sugaya I, Takahata H, Nomura H, et al. Brain 5alpha-dihydroprogesterone and allopregnanolone synthesis in a mouse model of protracted social isolation. Proc Natl Acad Sci U S A. 2001;98:2849–54.

57. Sotnikova TD, Beaulieu J-M, Espinoza S, Masri B, Zhang X, Salahpour A, et al. The dopamine metabolite 3-methoxytyramine is a neuromodulator. PLoS ONE. 2010;5: e13452.

58. Bittner S, Win T. Gupta R. gamma-L-glutamyltaurine. Amino Acids. 2005;28:343–56.

59. Figure 1. The kynurenine pathway. The first step is rate-limiting,... [Internet]. ResearchGate. https://www.researchgate.net/figure/The-kynurenine-pathway-The-first-step-is-rate-limiting-involving-tryptophan-getting_fig1_321675356. Accessed 7 Feb 2023.

60. Quinolinic Acid—an overview | ScienceDirect Topics [Internet]. https://www.sciencedirect.com/topics/neuroscience/quinolinic-acid. Accessed 7 Feb 2023.

61. Klein C, Patte-Mensah C, Taleb O, Bourguignon J-J, Schmitt M, Bihel F, et al. The neuroprotector kynurenic acid increases neuronal cell survival through neprilysin induction. Neuropharmacology. 2013;70:254–60.

62. Kynurenic acid in neurodegenerative disorders—unique neuroprotection or double-edged sword? Ostapiuk-2022-CNS Neuroscience & Therapeutics-Wiley Online Library. https://doi.org/10.1111/cns.13768

63. Csupor D, Tóth B, Mottaghipisheh J, Zangara A, Al-Dujaili EAS. Chapter 15—the psychopharmacology of saffron, a plant with putative antidepressant and neuroprotective properties. In: Ghosh D, editor. Nutraceuticals brain health beyond. Cambridge: Academic Press; 2021. p. 213–26.

64. Pieringer J, Keech S, Pieringer RA. Biosynthesis in vitro of sialosyl-galactosyldiacylglycerol by mouse brain microsomes. J Biol Chem. 1981;256:12306–9.

65. Ulivi V, Lenti M, Gentili C, Marcolongo G, Cancedda R, Descalzi CF. Anti-inflammatory activity of monogalactosyldiacylglycerol in human articular cartilage in vitro: activation of an anti-inflammatory cyclooxygenase-2 (COX-2) pathway. Arthritis Res Ther. 2011;13:R92.

66. Miller FW. The increasing prevalence of autoimmunity and autoimmune diseases: an urgent call to action for improved understanding, diagnosis, treatment, and prevention. Curr Opin Immunol. 2023;80: 102266.

Publisher's Note

Springer Nature remains neutral with regard to jurisdictional claims in published maps and institutional affiliations.